ACS Sustainable Chemistry & Engineering

pubs.acs.org/journal/ascecg

Research Article

Agricultural Wastes for Full-Cell Sodium-Ion Batteries: Engineering Biomass Components to Maximize the Performance and Economic Prospects

Qing Jin,[‖] Lei Tao,[‖] Yiming Feng, Dawei Xia, Glenn Allen Spiering, Anyang Hu, Robert Moore, Feng Lin, and Haibo Huang*

Cite This: *ACS Sustainable Chem. Eng.* 2023, 11, 536−546

Read Online

ACCESS | Metrics & More | Article Recommendations | Supporting Information

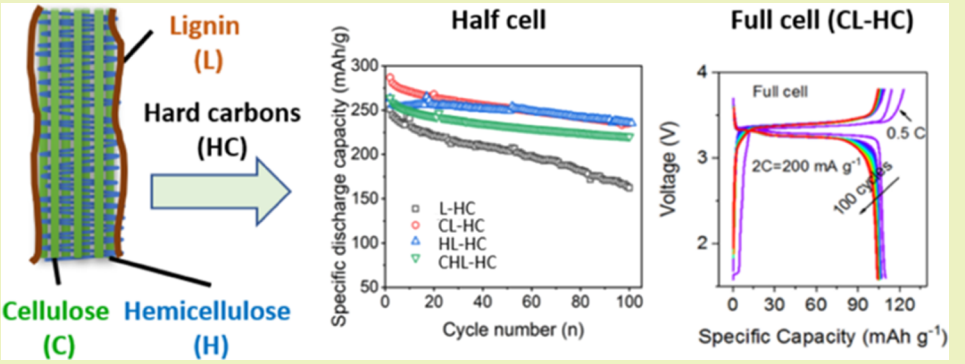

ABSTRACT: Lignin is one of the most abundant biopolymers in nature. Although lignin-derived hard carbon (L-HC) has potential to be used as a sodium-ion battery (SIB) anode but is limited by its poor electrochemical performance. In nature, lignin normally coexists with cellulose and hemicellulose in agricultural biomass, and studies have applied different agricultural biomasses to make SIB anodes; however, the underlying mechanism, especially the functionality of each component, is still unclear. In this study, we aim to combine lignin with cellulose and/or hemicellulose to produce hard carbons with outstanding electrochemical performance and low cost, and more importantly, unveil the underlying mechanisms. We found that the poor electrochemical performance of L-HC was mainly due to its large surface area with high amount of oxygen-containing functional groups and its unique physical structure that inhibit effective Na diffusion. Combining lignin with either cellulose or hemicellulose led to significantly improved electrochemical performance of the resulting hard carbon, with cellulose mainly contributing to the increase of capacity and hemicellulose mainly contributing to the stability of capacity during cycling and at high current density. Based on the comprehensive consideration of both electrochemical performance (half and full cells) and economic perspectives, lignin combined with cellulose showed great potential. Our study shed light on the contributions of each major biomass component on physical and electrochemical properties of resulting hard carbon and designed a unique way to improve L-HC.

KEYWORDS: *sodium-ion battery, cellulose, hemicellulose, lignin, hard carbon, economy*

INTRODUCTION

Energy storage technology has been flourishing in recent years to decrease reliance on fossil fuels. Lithium-ion batteries (LIBs) are considered as one big scientific breakthrough in the last 30 years.[1] However, there are increasing concerns regarding the limited availability and uneven distribution of required raw materials such as lithium and cobalt.[2,3] Compared with LIBs, sodium-ion batteries (SIBs) have indispensable advantages such as natural abundance, low cost of sodium, and high compositional tolerance of sodium cathodes to incorporate transition metals other than cobalt.[4−6] However, graphite, which is used in LIB anodes, is no longer suitable for SIBs due to unfavorable formation energy of Na−graphite intercalation compounds (GICs) compared to that of Li.[7,8] Therefore, finding promising and suitable anode materials is critical for the development of SIBs.

Instead of ordered carbon (graphite), disordered carbon, for example, hard carbon has shown promising electrochemical features such as low operating potential and considerable reversible capacity though the underlying storage mechanism

Received: August 8, 2022
Revised: December 20, 2022
Published: December 30, 2022

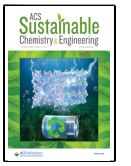

remains elusive, including adsorption, intercalation, pore filling, or combination of them. More importantly, hard carbons are produced from diverse sources.[9−12] For example, reed straw,[13] corncob and peanut shell,[14] brewer spent grain, walnut shell, and grape pomace,[15] corn straw,[16] citrus peels,[17] rape seed,[18] and lotus stem[19] have been carbonized into hard carbon with specific capacities ranging from 100 to 370 mAh/g. The diverse capacities from different biomass materials lead to the question of the role of each biomass component in determining the battery's electrochemical performance. In addition, there is lack of detailed analysis of the relationship between biomass-derived hard carbon composition/structure and SIB performance. Nevertheless, the seasonal availability and inconsistent composition of agricultural wastes would be against the electrochemical quality of derived hard carbon and thus impose challenges on consistently large-scale production.

Lignin is the second most abundant biopolymer in nature. It is also the main byproduct generated in the paper and pulp industry, and thus, it is a low-cost biomass with a consistent year-round supply. Moreover, lignin is composed of carbon-rich aromatic rings, making it a very attractive candidate for high yield. However, previous studies found that raw lignin-derived hard carbon fails to deliver good electrochemical performance, such as low initial coulombic efficiency and significant capacity decay.[20,21] Therefore, chemical modifications (e.g., nitrogen doping, preoxidation) and structure re-engineering of lignin (e.g., electrospinning to produce lignin nanofiber) were conducted to improve the structural and chemical properties of lignin-derived hard carbon as a SIB anode.[20−26] Nevertheless, these processes are not only tedious but are also adding additional processing cost to hard carbon production. Co-carbonization of lignin with other materials potentially endows a positive synergistic effect between lignin and the other materials via one-step synthesis. Recent work demonstrated that lignin combined with pitch and epoxy resin led to improved electrochemical performance.[27,28] However, both pitch and epoxy resin are nonrenewable petroleum-based products and have sustainability concerns when they are used to produce battery anodes at a large scale.

In this study, we aim to use cellulose and/or hemicellulose as additives to mix with lignin and produce hard carbon materials with outstanding electrochemical performance. Compared with petroleum-based precursors (e.g., pitch and epoxy resin), cellulose and hemicellulose are biorenewable and have a relatively low cost. In fact, cellulose and hemicellulose, together with lignin, are the three most abundant components in plant-based biomass; and they hold distinct elemental, structural, and thermochemical properties, which, in turn, provide grand opportunities to produce high-performance hard carbon by taking the advantages of these three components. Moreover, as previously mentioned, hard carbons derived from agricultural biomass containing different fractions of lignin, cellulose, and hemicellulose have a wide range of specific capacities but the underlying mechanisms are still unclear. Identifying the functionality of each of the three components and their synergistic effect on battery performance will provide critical information to guide the selection of appropriate biomass to produce high-performance hard carbon.

From our study, we found that lignin-derived hard carbon showed poor electrochemical performance (e.g., capacity decay, low capacity at high current density). This was mainly due to its high specific surface area with oxygen-containing functional groups reacting with an electrolyte to form a thick solid electrolyte interface (SEI) and unique physical structure (different sizes of globular structure with pores on the surface) that inhibits effective Na diffusion. However, when lignin is supplemented with either cellulose or hemicellulose for carbonization, its certain electrochemical performance was improved, with cellulose mainly contributing to the increase of capacity and hemicellulose mainly contributing to the stabilizing of cycling capacity. Our study indicates that cellulose, hemicellulose, and lignin contributed differently to the electrochemical properties of derived hard carbon and enables better designs of hard carbon by rationally selecting different biomass components to optimize the battery performance.

MATERIALS AND METHODS

Synthesis of Cellulose, Hemicellulose, and Lignin-Derived Hard Carbon. Cellulose (avicel cellulose) was purchased from Sigma-Aldrich (St. Louis, MO). Hemicellulose (xylan from corn core) was obtained from ALFA Chemistry, Protheragen Inc. (NY). Lignin (alkaline, L0082, derived from natural sources) was purchased from TCI America (Portland).

Lignin was carbonized individually or mixed thoroughly with the other two components before carbonization. The samples were placed in a tube furnace under constant nitrogen flow. The carbonization temperature and the temperature ramping rate were set at 1400 °C and 5 °C/min, respectively. The derived carbons included lignin-derived hard carbon (L-HC), lignin and hemicellulose mixed at a mass ratio of 1:1 derived hard carbon (HL-HC), cellulose and lignin mixed at a mass ratio of 1:1 derived hard carbon (CL-HC), and cellulose, hemicellulose, and lignin mixed at a mass ratio of 1:1:1 derived hard carbon (CHL-HC).

Carbon Characterization. The morphology of hard carbons was characterized using a scanning electron microscope (JEOL IT-500HR, JEOL, Tokyo, Japan). An automatic physical adsorption apparatus (ASAP 2020 Plus HD88, Micromeritics Co., Ltd.), operating temperature at −196 °C after being outgassed at 200 °C for 12 h under vacuum, was used to measure the specific surface area of hard carbons. The Bruker−Emmett−Teller (BET) method and pore size distribution from the adsorption branches of the isotherms using the density functional theory (DFT) method were applied. The polymorphism of hard carbon was measured using X-ray diffraction (XRD, Shimadzu, Japan) with Cu Kα (wavelength λ = 0.15406 nm). Raman measurements were performed using a WITec alpha500R instrument with a 532 nm excitation source. X-ray photoelectron spectroscopy (XPS) characterization was performed with a scanning photoelectron spectrometer microprobe (PHI Quantera SXM, ULVAC-PHI Inc., Japan), which was composed of an Al anode as the monochromatized X-ray source to obtain the surface elemental composition and valence state. The electrodes were soaked with flooded dimethyl carbonate (DMC) for 15 min, and then, they were dried naturally in a glovebox and loaded onto an XPS sample holder with O-ring sealing. Fourier transform infrared (FTIR) spectroscopy was applied to identify the functional groups, and spectra in the range of 500−4000 cm^{-1} with a resolution of 4 cm^{-1} were recorded. Skeletal density data were recorded on a Micromeritics AccuPyc 1340 pycnometer using a 1 cm^3 insert and an equilibration rate of 0.03 psig/min. Helium was used as the analysis gas. Closed pore volume was calculated as follows: $V_c = (1/\rho_s) - (1/\rho_g)$ where V_c is the closed pore volume, ρ_s is the skeletal density of the hard carbon, and ρ_g is the density of graphite, 2.26 g/cc.[29,30] Small-angle X-ray scattering (SAXS) experiments were performed using a Xeuss 3.0 SAXS/WAXS beamline, equipped with a GeniX 3D Cu HFVLF microfocus X-ray source with a wavelength of 0.154 nm (Cu Kα). The sample-to-detector distance was 900 mm for SAXS, 370 mm for mid-angle X-ray scattering (MAXS), and 43 mm for wide-angle X-ray scattering (WAXS). The q-range was calibrated using a lanthanum hexaboride standard for WAXS and a silver behenate standard for SAXS and MAXS. Two-dimensional scattering patterns were obtained using a Dectris EIGER 4M detector, with an exposure time of 2 h for SAXS, 1 h for MAXS, and 30 min for WAXS. The scattering data were reduced and

https://doi.org/10.1021/acssuschemeng.2c04750
ACS Sustainable Chem. Eng. 2023, 11, 536−546

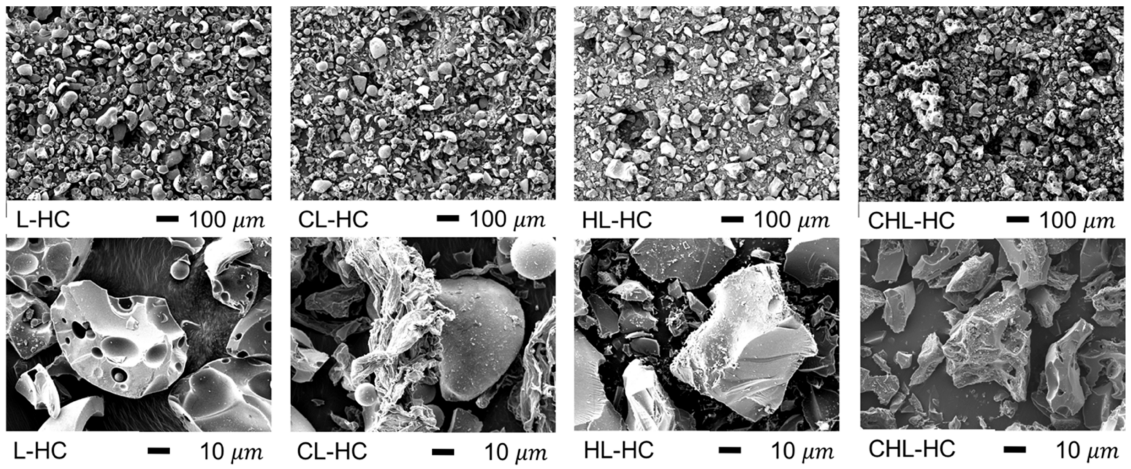

Figure 1. Morphology comparison of L-HC, CL-HC, HL-HC, and CHL-HC (carbonization temperature at 1400 °C). SEM magnification of ×100 for the first line and ×1000 for the second line. L-HC showed a globular structure with different sizes and some with pores both on the surface and inside of particles, while this structure does not appear on HL-HC and CHL-HC, as they formed irregular bigger chunks. For CL-HC, it seemed that they were resistant to merge, and their unique morphologies remained; meanwhile, smaller cellulose strips and lignin with less pores were observed.

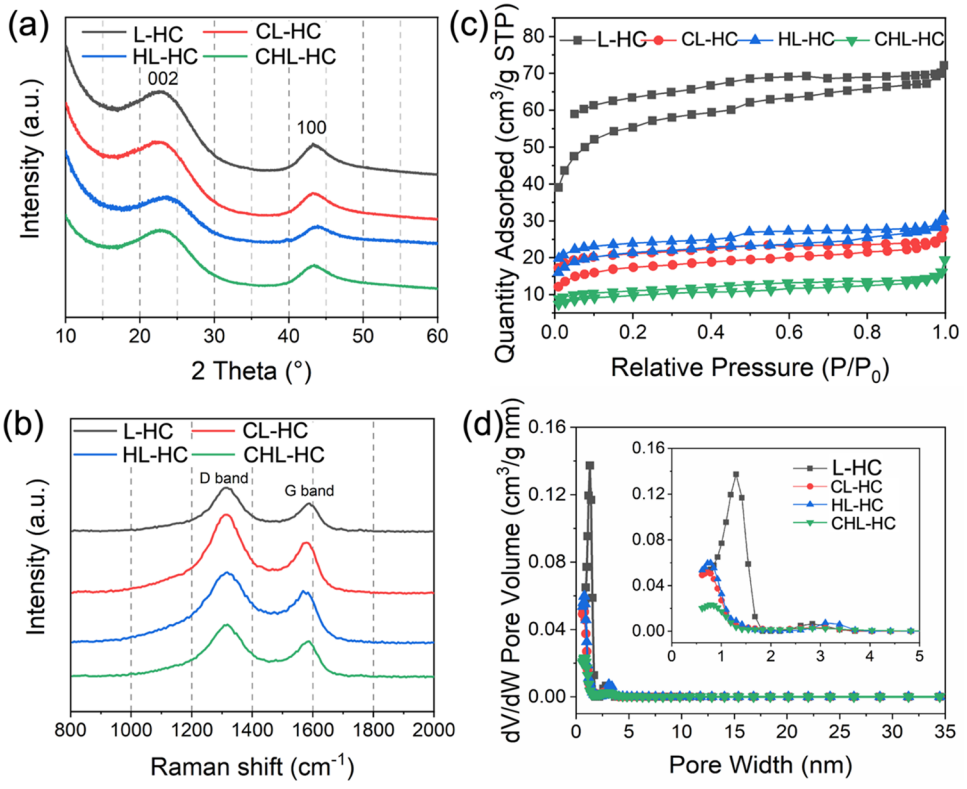

Figure 2. (a) XRD patterns of hard carbon materials of L-HC, CL-HC, HL-HC, and CHL-HC. L-HC, CL-HC, and CHL-HC showed similar d_{002} with a range of 0.382−0.384 nm, but the (002) peak (0.373 nm) of HL-HC shifted to a higher diffraction angle compared with other carbons, indicating the formation of more graphitic structure compared with others. (b) Raman spectrum of hard carbon materials. HL-HC showed the lowest I_D/I_G ratio of 1.93, indicating that this combination had less defected carbon but more graphitic carbon. (c) N_2 adsorption/desorption isotherms of hard carbon materials. L-HC showed the highest BET surface area of 161.201 m^2/g, CHL-HC showed the lowest surface area of 30.374 m^2/g, and others were in the range of 50−60 m^2/g. (d) Pore size distribution. All samples showed micropores, and for L-HC and HL-HC, there were a small amount of mesopores in the range of 2−4 nm.

corrected for background and transmission using XSACT software. SAXS, MAXS, and WAXS profiles were merged using XSACT software. The scattering profiles were vertically shifted to facilitate comparison. Scattering plots are presented as scattering intensity, $I(q)$, versus scattering vector q, where $q = (4\pi/\lambda)\sin(\theta)$, θ is one half of the scattering angle, and λ is the X-ray wavelength. Scattering curves were analyzed by Irena software using the unified fit equation to extract pore size as radius of gyration. Assuming spherical pores, the pore diameter was calculated as $D = 2\sqrt{5/3}\ R_g$, where D is the pore diameter and R_g is the radius of gyration.[31−33]

Electrochemical Characterization. For half-cell testing, the electrodes were made by mixing produced hard carbon with a poly(tetrafluoroethylene) binder and carbon black in a mass ratio of 8:1:1 on a copper foil. The electrodes were cut into a circular shape with a diameter of 12 mm, followed by drying at a 121 °C vacuum oven

https://doi.org/10.1021/acssuschemeng.2c04750
ACS Sustainable Chem. Eng. 2023, 11, 536−546

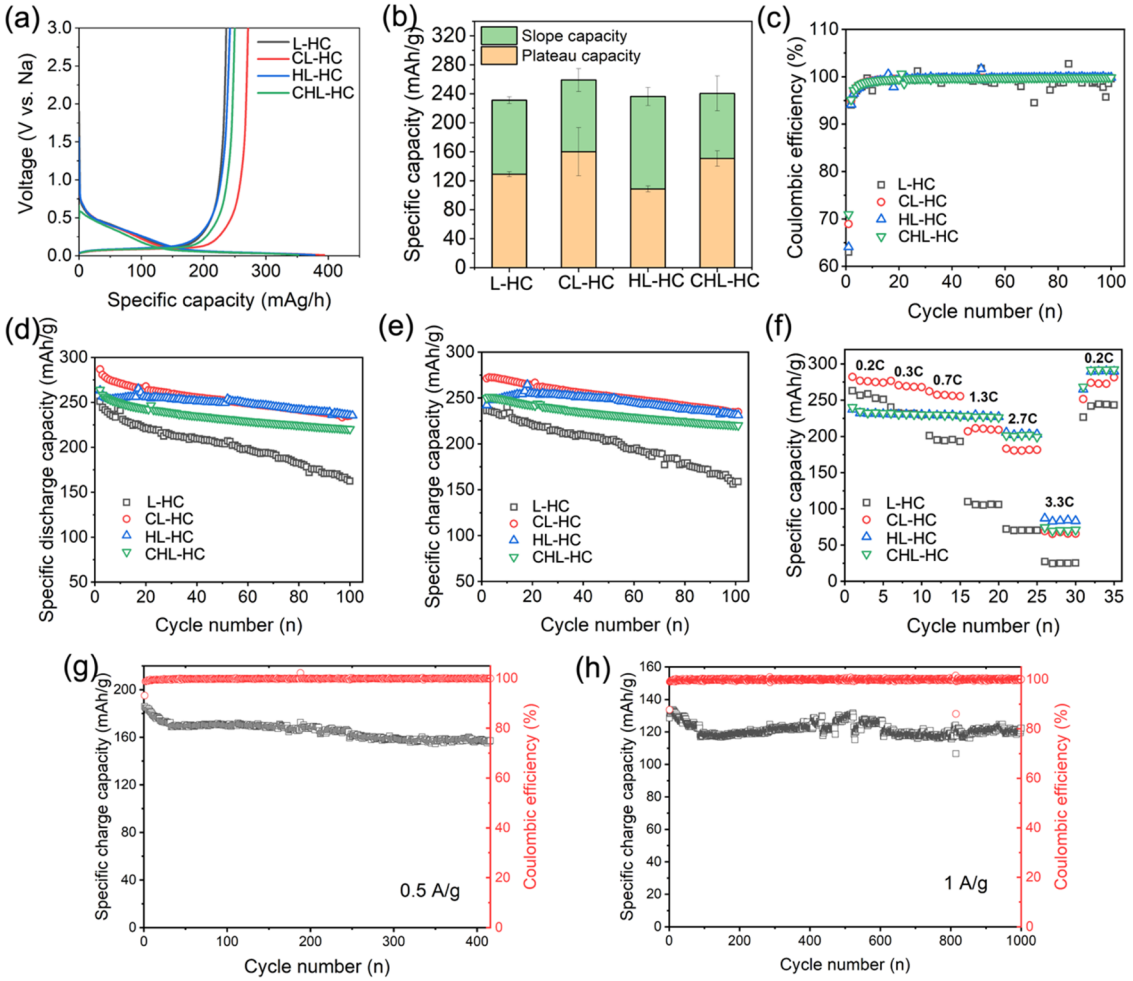

Figure 3. (a) Galvanostatic first discharge/charge profiles of L-HC, CL-HC, HL-HC, and CHL-HC derived electrodes in half cells at a current rate of 100 mAh/g, in which CL-HC showed the highest specific charging capacity. (b) Contribution of plateau and slope capacity (duplicates), in which CL-HC and CHL-HC showed higher plateau capacity compared with that of L-HC and HL-HC. (c) Coulombic efficiency, in which CL-HC and CHL-HC showed higher initial columbic efficiency compared with that of L-HC and HL-HC. (d) Discharge cycling curves, in which L-HC showed remarkable decay compared with others. (e) Charge cycling curves, in which L-HC showed remarkable decay compared with others. (f) Rate capability of different hard carbon-derived electrodes, in which CL-HC showed good specific capacity at a current density from 0.2 to 0.7C (1C = 300 mA/g); HL-HC and CHL-HC held capacity better at a higher density from 1.3 to 3.3C; L-HC showed remarkable lower specific capacity at higher current density. (g) Long-term cycling of CL-HC at 0.5 A/g (1.7C). (h) Long-term cycling of CL-HC at 1 A/g (3.3C).

overnight. The mass loading of the active material was ~2 mg. A sodium metal was used as the counter electrode and 1 M $NaPF_6$ in diglyme was used as the electrolyte. A piece of glass fiber (GF/D 47, Whatman) was placed between the electrode and Na metal serving as a separator. The battery assembly was operated in an argon-filled glovebox. Galvanostatic cycling tests were carried out using a battery tester (NEWARE, Shen Zhen, China) in a voltage range of 0.01−3 V (vs Na^+/Na). Cyclic voltammetry (CV) tests were performed between 0.01 and 3 V (vs Na^+/Na) using a multichannel potentiostat−galvanostat. All electrochemical tests were performed at 22 °C. The galvanostatic intermittent titration technique (GITT) was employed in hard carbon half-cells after activation. The resting period was 6 h while the pulse time was 30 min. The current density was 0.1 A/g. For spherical particles, the ion diffusion coefficient (D) was calculated following a previous paper.[34]

For full-cell testing, the cathode was prepared by mixing the $Na_3V_2(PO_4)_3$ (NVP) active material, carbon black, and PVDF (at a mass ratio of 9:0.5:0.5) in NMP solvent to form a slurry, and then drop-cast on a carbon-coated aluminum foil. The prepared cathode was punched into 10 mm diameter disks and dried overnight in a vacuum oven at 120 °C. The mass loading of the active material was 3−4 mg. The full cell was assembled using NVP as the cathode, 1 M $NaPF_6$ in diglyme as the electrolyte, glass fiber as the separator, and hard carbon or presodiation carbon as the anode. To eliminate the irreversible Na inventory loss caused by the parasitic electrode−electrolyte reactions, the pristine CL-HC electrode was chemically presodiated in a 0.2 M Na biphenyl solution (Na-Bp-Diglyme) for several minutes and then washed with diglyme solvent, yielding presodiated CL-HC. Cyclic voltammetry (CV) tests were performed between 1.6 and 3.8 V (vs Na^+/Na). All electrochemical tests were performed at 22 °C.

RESULTS AND DISCUSSION

Synthesis and Characterization of Hard Carbons. Lignin showed the highest carbon yield of 37.1% during carbonization, and combining lignin with cellulose and hemicellulose decreased the carbon yield to 24.7−25.8%. These results reflect the higher stability of lignin during carbonization compared with cellulose and hemicellulose (Table S1). The morphology (SEM) of these hard carbons is shown in Figure 1. We can see that L-HC showed a globular structure with different sizes and some with pores both on the surface and inside of particles, but this structure does not appear on HL-HC and CHL-HC, which showed irregular bigger flakes. For CL-HC, it appears that cellulose and lignin were resistant to merge, and their unique morphologies remained (Figure 1); meanwhile,

https://doi.org/10.1021/acssuschemeng.2c04750
ACS Sustainable Chem. Eng. 2023, 11, 536−546

smaller cellulose strips and lignin granules with less pores were observed.

Figure 2a shows the XRD results, and all hard carbons showed two broad peaks of 002 (2θ = 22°) and 100 (2θ = 43°), which are typical for disordered carbon. Among these hard carbons, L-HC, CL-HC, and CHL-HC showed similar d_{002} with a range of 0.382−0.384 nm (Table S1). The (002) peak of HL-HC shifted to a higher diffraction angle with a decreased interlayer spacing (d_{002} = 0.373 nm) of the graphene sheets, indicating the formation of more graphitic structure of HL-HC compared with other hard carbons. Figure 2b compares the Raman spectrum of all derived hard carbons. The two characteristic bands at around 1340 and 1580 cm^{-1} are attributed to the D band (disordered sp^3 carbon/defected carbon) and G band (ordered sp^2 carbon/graphitic carbon), respectively. The peak intensity ratio (I_D/I_G) indicates the carbon materials' disorder.[35] Among the four samples, HL-HC had the lowest I_D/I_G ratio of 1.93, indicating that the combination of lignin and hemicellulose resulted in less defected carbon but more graphitic carbon, which is consistent with the XRD results.

As to nitrogen adsorption−desorption measurements (BET and porosity) (Table S1 and Figure 2c,d), L-HC had the highest surface area of 161 m^2/g and CHL-HC had the lowest surface area of 30 m^2/g. The surface areas of other hard carbons were in the range of 50−60 m^2/g. The large surface area of L-HC could be due to its globular structure with different sizes of pores on the surface as shown in SEM (Figure 1). The DFT pore size distribution showed the existence of micropores for all hard carbons (Figure 1d). There was a small amount of mesopores with a range of 2−4 nm in L-HC and HL-HC. Dead pore volume was obtained from helium psychometry. HL-HC showed the largest closed pore volume (0.1107 cc/g), followed by CHL-HC (0.0493 cc/g), CL-HC (0.0177 cc/g), and L-HC (0.0121 cc/g) (Table S2). The higher closed pore volume could be due to hemicellulose coating on lignin during carbonization, which may cover up open pores on lignin and turn them into closed pores (Figure 1). For CL-HC, it seems that cellulose was resistant to be coated on lignin with the evidence that small cellulose strips and lignin with open pores were observed (Figure 1). Dead pore diameter was measured using SAXS (Figure S1 and Table S3). HL-HC showed the highest closed pore diameter of 2.59 nm. Closed pore diameters for the other hard carbons were about 2 nm. The closed pore diameter measured herein was the diameter of dead pores/cavity between graphite carbons, and the high closed pore diameter of HL-HC might be due to its formation of more graphitic carbon verified by XRD and Raman.

The specific surface area and closed pores were different after adding cellulose and hemicellulose. The high surface area and low closed pores of L-HC could result in a high adsorption capacity (>0.1V) and meanwhile a low ICE (Tables S1 and S2). Combined with cellulose and hemicellulose, the surface area decreased, and the closed pore increased, which was suitable for Na^+ intercalation and could provide an impressive electrochemical performance.

As to the elemental composition characterized by XPS, we found that L-HC showed less amount of carbon (75.7%) than C-HC (88.9%) and H-HC (89.1%) while almost doubled the amount of oxygen (16.7%) than the other two. The higher oxygen content in lignin-derived hard carbon might be due to the fact that lignin is more thermochemically stable and resistant to be carbonized compared with cellulose and hemicellulose. The higher content of oxygen, the more potential formation of oxygen-containing functional groups, which might lead to degradation of electrolytes and could further lead to the difference in adsorption capacity of SIBs.[36]

To summarize, among L-HC, CL-HC, HL-HC, CHL-HC samples, L-HC has the highest yield and specific surface area and lowest closed pore volume. Lignin combined with hemicellulose-derived hard carbon (HL-HC) had more graphitic carbon, smaller interlayer space, and highest closed pore volume and diameter compared with others. From the elemental perspective, L-HC showed the highest O content, and by mixing cellulose or hemicellulose, the O content could be reduced. In addition, they all showed diverse morphology. All of these lead to their different electrochemical and economic performance as we will discuss in the following sections.

Electrochemical Characterization of Hard Carbons in Half Cells. We assembled the hard carbons into Na-ion half cells to measure the electrochemical performances. Figure 3a shows the first galvanostatic discharge/charge curves at a current density of 100 mA/g. The CL-HC sample showed the highest reversible capacity of 259 mAh/g, followed by CHL-HC (240 mAh/g), HL-HC (236 mAh/g), and L-HC (231 mAh/g). The capacities were in a reasonable range compared with previous studies.[14,15] As to the distribution of plateau and slope capacity, CHL-HC and CL-HC showed a higher percentage of plateau capacities of 62.8 and 61.8%, respectively, than L-HC (55.8%) and HL-HC (46.0%) did (Figure 3b). To understand the sodium storage mechanisms in the hard carbons, cyclic voltammetry (CV) with varying scanning rates was conducted, followed by curve fitting to interpret pseudocapacitive Na^+ storage and diffusive Na storage (Figure S2).[15,37−39] The anodic and cathodic peak currents in the plateau region were assigned as P and P′, and the anodic and cathodic peak currents in the slope region were assigned as S and S′. The curve fitting between current and scan rates was based on the formulation: $i = a \times v^b$. If b is close to 1, it indicates a surface mass transport with fast kinetics, while if b is close to 0.5, it indicates a bulk mass transportation with slow kinetics.[15,39] L-HC and CL-HC were selected as representative hard carbons, and based on our results, both of them showed b value close to 0.5 in the plateau region and close to 1 in the slope region, indicating a predominant Na surface adsorption mechanism in the slope region and a predominant Na intercalation mechanism in the plateau region, which was in accordance with some previous studies stating that the slope capacity could be attributed to the Na-ion storage at surface and defect sites, edges of hard carbon, while the plateau capacity was attributed to Na-ion intercalation between graphene layers (d_{002}) and storage in the closed voids in hard carbon.[40−43] From the previously discussed possible mechanisms, the higher capacity of CL-HC and CHL-HC could be ascribed to the larger interlayer spaces (d_{002}) and more defects (I_D/I_G), which are beneficial to Na storage, and the slightly lower capacity of L-HC and HL-HC could be ascribed to their smaller interlayer spaces and less defects (Table S1).

The initial coulombic efficiencies (ICEs) of CL-HC and CHL-HC were higher (69−70%) than those of L-HC and HL-HC (64−65%) (Figure 3c). The reason for the low initial coulombic efficiency of L-HC was mainly due to its large surface area with high amount of oxygen-containing functional groups and other impurities (Tables S1 and S4), which could react with the electrolyte to form SEI, resulting in a low initial coulombic efficiency.[15,44] As to HL-HC, even though the surface area was low, it had the highest amount of closed pore volume, which might be one possible reason causing the low ICE (Table S2). The coulombic efficiency of CL-HC and CHL-HC gradually

https://doi.org/10.1021/acssuschemeng.2c04750
ACS Sustainable Chem. Eng. 2023, 11, 536−546

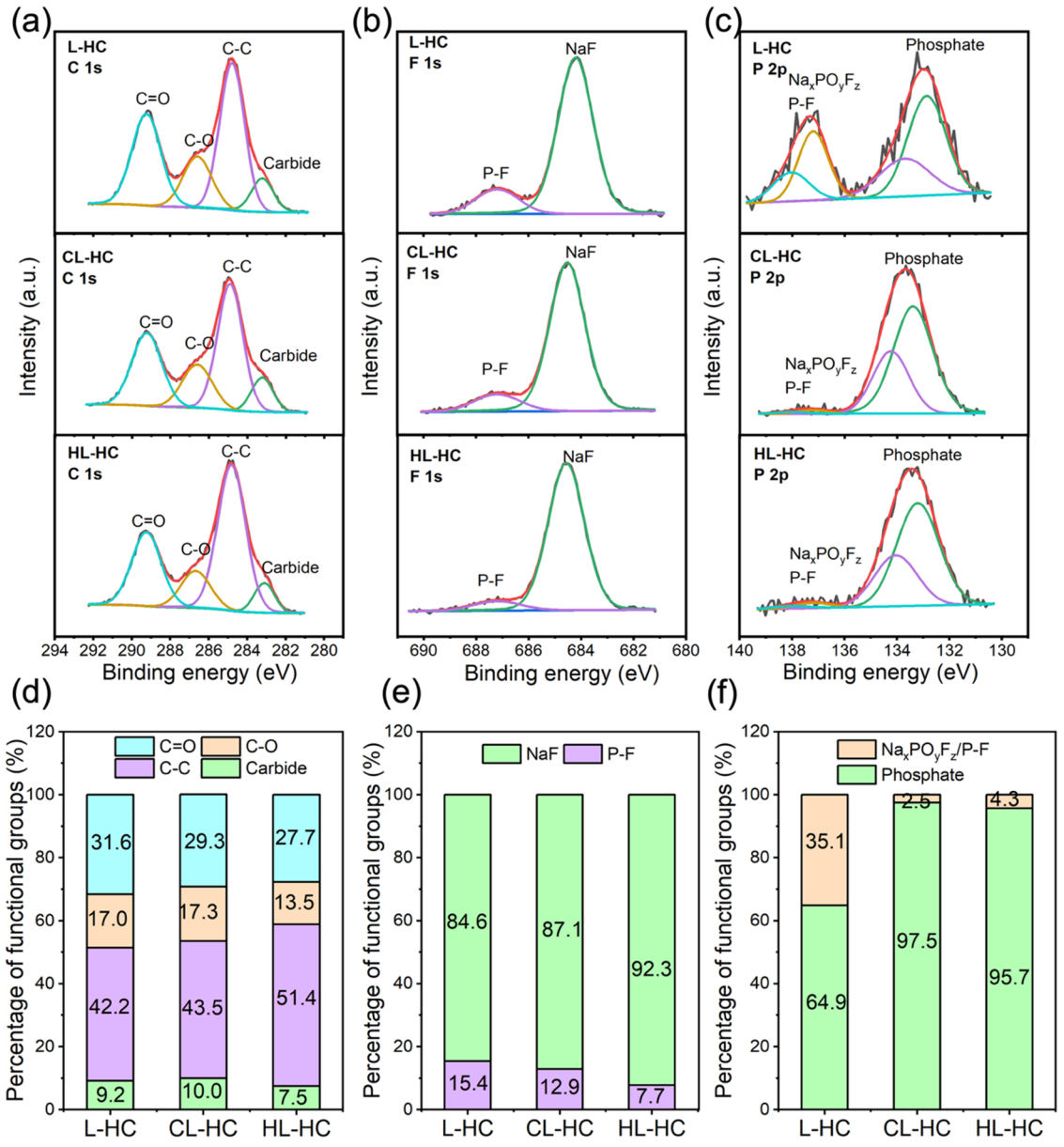

Figure 4. XPS deconvoluted spectra after 100 cycles for L-HC, CL-HC, and HL-HC. (a) High-resolution C 1s spectrum of L-HC, CL-HC, and HL-HC. (b) High-resolution F 1s spectrum of L, CL-HC, and HL-HC. (c) High-resolution P 2p spectrum of L-HC, CL-HC, and HL-HC. (d) Percentage of C 1s functional groups, in which L-HC showed a higher percentage of C═O compared with that of CL-HC and HL-HC. (e) Percentage of F 1s functional groups, in which L-HC showed a lower amount of NaF compared with that of CL-HC and HL-HC. (f) Percentage of P 2p functional groups, in which L-HC showed a remarkably higher amount of $Na_xPO_yF_z$/P-F compared with that of CL-HC and HL-HC.

increased to over 99.7% and remained stable during the 100 cycles. However, the coulombic efficiency of L-HC and HL-HC showed fluctuations, which might be due to their poor surface and structure properties (Figure 3c).

Figure 3d,e shows the discharge/charge curves during the first 100 cycles, with CL-HC and CHL-HC showing a similar decreasing trend. As to HL-HC, there was a slight increase of the capacity during the first 20 cycles, followed by a decrease of capacity, which might be due to its higher closed pore volume and diameter, indicating that HL-HC needs more time to be activated and stabilized (Table S2). L-HC had a similar capacity, decreasing trend as CL-HC and CHL-HC, but its capacity decay was much higher in both slope and plateau capacity decay (around 30−40%) (Figure S3). One possible reason for the high capacity decay of L-HC could be attributed to its large surface area and associated with high amount of oxygen-containing functional groups (Tables S1 and S2). We further applied XPS to investigate the electrolyte decomposition products on the electrode surface films after 100 cycles (Figure 4). From the overall atomic concentration, we found that L-HC had higher atomic O (30.5%) compared with CL-HC (29.4%) and HL-HC (27.6%), and moreover, L-HC had lower C/O, F/O, and P/O ratios compared with those of CL-HC and HL-HC (Table S5). From the C 1s spectrum, four peaks were observed in all samples at binding energies of 283.21, 284.79, 286.59, and 289.24 eV, which were associated with carbide, C−C, C−O, and C═O groups, respectively (Figure 4a). However, the percentage share of these groups was different: L-HC had a higher percentage of C═O than CL-HC and HL-HC had (Figure 4d). As to the F 1s spectrum, two peaks were found at binding energies of 684.18

https://doi.org/10.1021/acssuschemeng.2c04750
ACS Sustainable Chem. Eng. 2023, 11, 536−546

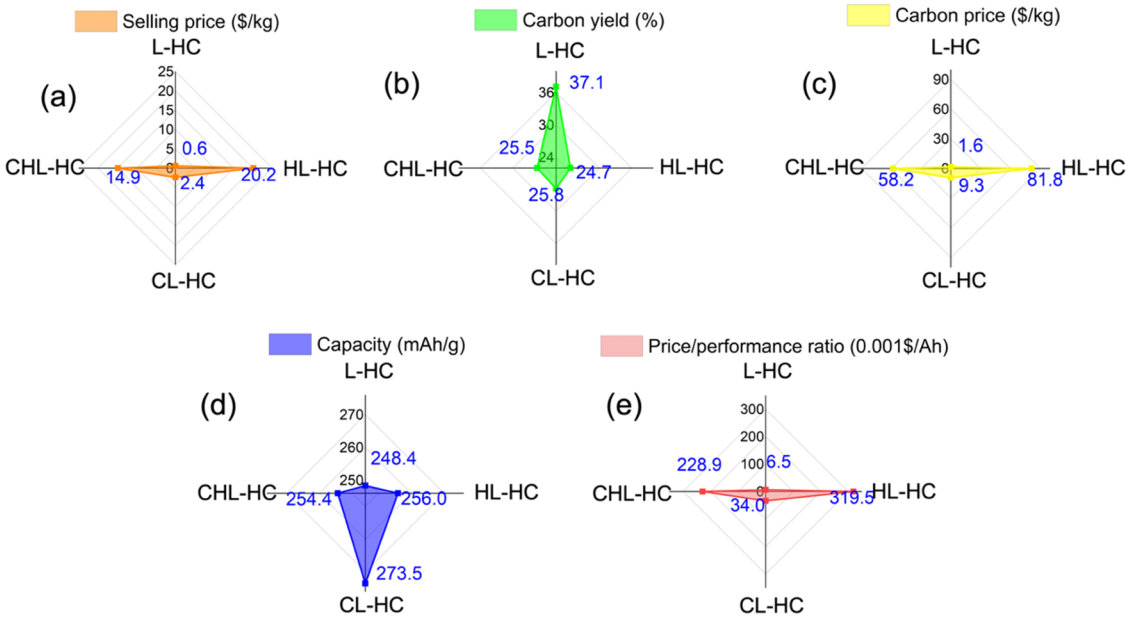

Figure 5. Major properties of L, CL-HC, HL-HC, and CHL-HC derived hard carbons for anodes of sodium-ion battery. (a) Selling price of raw materials (cellulose: $4.5/kg, hemicellulose: $39.8/kg, lignin: $0.6/kg) based on 2021 U.S. market. (b) Yield of hard carbon generated from raw materials. (c) Hard carbon price calculated based on the selling price of raw materials and hard carbon yield. (d) Average specific first charging capacity of hard carbon (current density at 100 mA/g). (e) Hard carbon price to average specific first charging capacity ratio of different hard carbons, the lower the ratio, the higher the potential to be used in real practice.

and 686.99 eV, which were assigned to P-F and NaF, respectively (Figure 4b). Compared with CL-HC and HL-HC, L-HC showed a lower amount of NaF (Figure 4e). Previous research analyzed the relationship between the chemical composition of SIB electrode's SEI and the electrochemical performance and reported that poor electrochemical performances were related to either high Na_2CO_3 or low NaF content in the electrode's SEI after cycling,[45] which supported our hypothesis that the poor electrochemical performance of L-HC is due to the low NaF in the formed SEI. As to the P 2p spectrum, two peaks at 132.88 and 137.21 eV were determined corresponding to phosphate and $Na_xPO_yF_z$/P-F, respectively (Figure 4c). The percentage contributions of these two groups were different, in which L-HC had a much higher amount of $Na_xPO_yF_z$/P-F than CL-HC and HL-HC had (Figure 4f). $Na_xPO_yF_z$/P-F are the compounds in SEI formed during cycling, and the higher percentage of $Na_xPO_yF_z$/P-F in L-HC indicates more reaction between the electrolyte and the functional groups of the hard carbon, and thus more SEI formation.[46,47] Overall, the results revealed that the poor electrochemical performance and high capacity decay of L-HC could be due to the formation of thick SEI during cycling.

To further understand the sodium-ion diffusion pattern in the hard carbon, we applied the galvanostatic intermittent titration technique (GITT) to calculate the Na-ion diffusion coefficient in L-HC, CL-HC, and HL-HC samples. The apparent diffusion coefficient of Na ions was computed according to Fick's second law (eq 1)

$$D_{Na^+} = \frac{4}{\pi\tau}\left(\frac{m_B V_M}{M_B S}\right)^2\left(\frac{\Delta E_s}{\Delta E_\tau}\right)^2 \quad (1)$$

where τ was the pulse duration, m_B was the active mass, V_M was the molar volume, M_B was the active mass, S was the active surface area, and ΔE_s and ΔE_τ were derived from the GITT curves.[48] The sodiation process pattern was similar for the L-HC, CL-HC, and HL-HC electrodes (Figure S4). The Na-ion diffusion coefficient at the sloping region was much higher than that at the plateau region, which was mainly due to the widely available defect sites, micropores, and vacancies.[13] As defects and micropores were gradually occupied, Na ions started implanting in the interlayer space of the graphite-like hard carbon, during which Na ions need to overcome high energy barriers, causing a sharp decrease of the apparent diffusion coefficient at the early stage of the plateau region. After Na ions intercalated into the interlayer space, the interlayer space was expanded, which benefits further Na-ion embedding process and results in an increased apparent diffusion coefficient at the late stage of the plateau region. It should be noted that the apparent diffusion coefficient of CL-HC and HL-HC was higher than that of the L-HC in both plateau and slope regions (Figure S4), which could be a possible reason for the improved electrochemical performance and capacity retention of CL-HC and HL-HC compared with L-HC.

We further evaluated the rate performance of the L-HC, CL-HC, HL-HC, and CHL-HC electrodes at various rates from 0.2 to 3.3C (1C = 300 mA/g) (Figure 3f). Among the four electrodes, CL-HC showed the highest capacity at current densities from 0.2 to 0.7C and then presented a similar level with HL-HC and CHL-HC when further increasing the current densities from 1.3 to 3.3C. As to HL-HC and CHL-HC, even though their capacities were lower than CL-HC and L-HC at a low current density, they retain well when the current density increased from 0.2 to 1.3C, and at a high current density of 1.3C, the capacities still hold at around 200 mAh/g, indicating that hard carbon blended with hemicellulose is beneficial for capacity retaining, especially at a high current density. Interestingly, as we reduced the current density back to 0.2C, both HL-HC and CHL-HC bounced back to around 290 mAh/g, slightly higher than their initial stage at 0.2C, indicating that more activation process is needed for hard carbon derived from the biomass-containing hemicellulose. The capacity of L-HC decayed quickly

https://doi.org/10.1021/acssuschemeng.2c04750
ACS Sustainable Chem. Eng. 2023, 11, 536−546

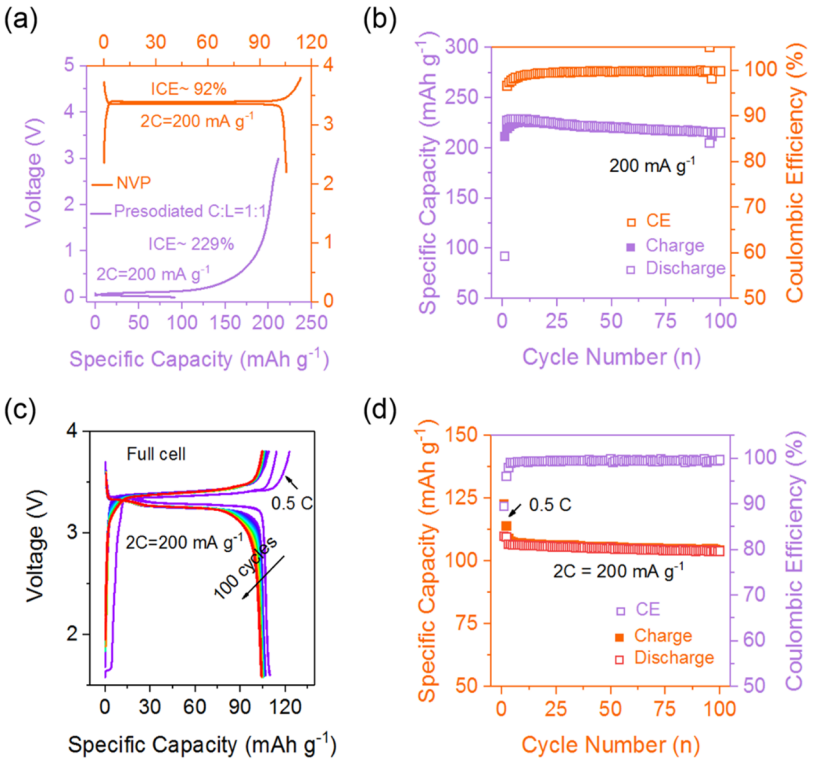

Figure 6. (a) First charge−discharge voltage profile of NVP||Na half-cell and presodiated carbon||Na half-cell at 2C (1C = 100 m Ag^{-1}). (b) Cycling stability of the persodiated carbon anode at 200 mAh/g. (c) Voltage profiles of NVP||persodiated carbon full cell at 2C for 100 cycles, where the full cell is activated with two cycles at 0.5C. (d) Corresponding cycling performance at 2C.

with the increasing current density, which might be related to thick SEI formation due to its high surface area and high amount of oxygen-containing functional groups and its particular structure that hindered Na transportation during cycling (Figures 1, 4 and S4 and Tables S1 and S4).

Finally, we also performed the long cycling of CL-HC at rates of 0.5 and 1.0 A/g. We could see that CL-HC exhibited an initial capacity of 186 mAh/g at 0.5 A/g, followed by a slight decrease during the first 50 cycles. After that, almost no capacity loss was observed, and a final capacity of 157 mAh/g could be obtained after 410 cycles. At 1 A/g, a similar trend was found. The initial capacity of CL-HC was 129 mAh/g, and CL-HC could still maintain a reversible capacity of 122 mAh/g after 1000 cycles (Figure 3g,h).

From previous results, we found that L-HC had poor electrochemical performance in terms of relatively low capacity, low initial columbic efficiency, high capacity decay during cycling, and poor capacity holding ability at high current density, which was mainly due to the high specific surface area, high oxygen-containing functional groups on the surface, other impurities reacting with electrolytes, and particular physical structure that inhibit effective Na diffusion. However, when lignin is mixed with either cellulose or hemicellulose for carbonization, its certain electrochemical performance property was improved, with cellulose mainly contributing to the increase of capacity and hemicellulose mainly contributing to the stability of capacity during cycling and at high current density. These findings indicate that cellulose, hemicellulose, and lignin have contributed differently to the resulting hard carbon as battery anode materials, and their different combination will affect the battery performance.

Economic Assessment. To have a comprehensive understanding of the material selection on the economics of hard carbon, several parameters were evaluated and considered together, which included the market selling prices of raw cellulose, hemicellulose and lignin, carbon yield, carbon price, capacity, and the final price/performance ratio of different hard carbons (Figure 5). The market selling prices of cellulose, hemicellulose, and lignin were set at $4.5/kg, $39.8/kg, and $0.6/kg, respectively, based on the mean selling price from the quotes of several companies (based on the year 2021 in the U.S. market). We could see that L-HC had the lowest price/performance ratio of $0.0065/Ah, followed by CL-HC ($0.034/Ah). Since hemicellulose had the highest selling price, any material blended with hemicellulose showed a relatively high price/performance ratio, indicating that hemicellulose may not be a good source to be used for sodium-ion anode production from the economic standpoint. Even though L-HC had the lowest price/performance ratio, the fast capacity decay of L-HC and the poor performance at high current density make L-HC not a good choice in real practice. Instead, CL-HC could be a good choice for further investigation and application.

Full Cell Performance. Due to the better electrochemical and economic performance of CL-HC, we further explored the practical application of the CL-HC anode in the full cell. When the capacity ratio of the pristine CL-HC anode to the $Na_3V_2(PO_4)_3$ (NVP) cathode is 1.2, the full cell cannot be cycled stably, and the capacity decays rapidly, which is caused by the low ICE of the CL-HC anode (Figure 3e). To compensate for the irreversible Na loss of the CL-HC anode, we adopt a facile and efficient chemical presodiation strategy to modify the anode side. Figure 6a shows the first charge−discharge profiles of the presodiated CL-HC anode and NVP cathode at 2C.

https://doi.org/10.1021/acssuschemeng.2c04750
ACS Sustainable Chem. Eng. 2023, 11, 536−546

Compared with the pristine CL-HC anode with a low ICE of 70%, the presodiated CL-HC anode delivers a high ICE of 229%, indicating that the irreversible Na has been completely compensated. Notably, the oversodiation of the CL-HC anode can not only ensure that there is sufficient Na source to compensate for the low CE of the anode in the next few cycles (lower than 90%) but also can compensate for the low ICE of the cathode (only 92%). Figure 6b shows the cycling stability of the presodiated CL-HC||Na half-cell at a current density of 200 mA/g. After 100 cycles, the presodiated CL-HC anode has a reversible capacity of 220 mA/g with a capacity retention of 95%, which is similar to the pristine CL-HC anode under the same conditions, indicating the feasibility of chemical presodiation. The presodiated CL-HC||NVP full cell is also assembled at a capacity ratio (N/P) of 1.2/1 (based on the CL-HC capacity to NVP capacity at the same current). As shown in Figure 6c,d, the cycling stability of the presodiated CL-HC||NVP full cell has been significantly improved. The presodiated CL-HC||NVP full cell has a high ICE and a stable charge−discharge plateau, indicating that the irreversible capacity is compensated (Figure 6c). After 100 cycles, the presodiated CL-HC||NVP full cell still has a high specific capacity of 104 mA/g with a capacity retention of 97%. As a result, the good electrochemical performance of the CL-HC anode in half and full cells together with its cost-effective economic performance illustrate its potential value in practical applications.

CONCLUSIONS

In this study, we have demonstrated that biowaste lignin supplemented with cellulose and hemicellulose could serve as an ideal precursor to produce hard carbon for the high-performance SIB anode. Due to its large surface area, high amount of oxygen-containing functional groups, and unique physical structure (different sizes of globular structure with pores on the surface) that inhibit effective Na-ion diffusion, the lignin-derived hard carbon had poor electrochemical performance as an SIB anode. However, by combining lignin with cellulose and hemicellulose, the derived hard carbon had a significantly improved electrochemical performance with the highest capacity of 259 mAh/g and about 80% of capacity retention after 100 cycling. The improved performance was mainly attributed to the expanded interlayer spaces and reduced surface area of the hard carbon. Moreover, we unveiled that cellulose mainly contributed to the increase of capacity during cycling and hemicellulose mainly contributed to the stability of capacity at high current densities. We further applied a comprehensive economic analysis of the hard carbon production and found that lignin combined with cellulose had great potential for further application. The practical feasibility of CL-HC in the full cell was further confirmed by combining with the $Na_3V_2(PO_4)_3$ (NVP) cathode, delivering a reversible capacity of 104 mA/g with a capacity retention of 97% after 100 cycles. In the future, the ratio of lignin, cellulose, and hemicellulose will be systematically investigated to identify the best mixture of the three components to achieve the optimal electrochemical and economic performances of hard carbon.

ASSOCIATED CONTENT

Supporting Information

The Supporting Information is available free of charge at https://pubs.acs.org/doi/10.1021/acssuschemeng.2c04750.

Yield and structural information of hard carbons (Table S1); closed pore information of hard carbons (Table S2); merged SAXS/MAXS/WAXS profiles of the hard carbons (Figure S1); radius of gyration (R_g) and Porod exponent (P) obtained from applying the unified fit function to the SAXS/MAXS/WAXS profiles of hard carbons (Table S3); elemental composition of hard carbons (Table S4); cyclic voltammetry (CV) curves of hard carbon-derived electrodes with varying rates and corresponding linear fitting (Figure S2); elemental composition of hard carbon-derived electrodes after cycling (Table S5); total, plateau, and slope capacity retentions of hard carbon-derived electrodes (Figure S3); and Na-ion apparent diffusion coefficients of hard carbon-derived electrodes (Figure S4) (PDF)

AUTHOR INFORMATION

Corresponding Author

Haibo Huang − *Department of Food Science and Technology, Virginia Polytechnic Institute and State University, Blacksburg, Virginia 24061, United States;* orcid.org/0000-0002-2106-4105; Phone: 540-231-0729; Email: huang151@vt.edu; Fax: (540) 231-9293

Authors

Qing Jin − *Department of Food Science and Technology, Virginia Polytechnic Institute and State University, Blacksburg, Virginia 24061, United States;* orcid.org/0000-0002-2377-5218

Lei Tao − *Department of Chemistry, Virginia Polytechnic Institute and State University, Blacksburg, Virginia 24061, United States*

Yiming Feng − *Department of Food Science and Technology, Virginia Polytechnic Institute and State University, Blacksburg, Virginia 24061, United States;* orcid.org/0000-0002-9693-3686

Dawei Xia − *Department of Chemistry, Virginia Polytechnic Institute and State University, Blacksburg, Virginia 24061, United States;* orcid.org/0000-0003-4265-2528

Glenn Allen Spiering − *Department of Chemistry, Virginia Polytechnic Institute and State University, Blacksburg, Virginia 24061, United States; Macromolecules Innovation Institute, Virginia Polytechnic Institute and State University, Blacksburg, Virginia 24061, United States*

Anyang Hu − *Department of Chemistry, Virginia Polytechnic Institute and State University, Blacksburg, Virginia 24061, United States;* orcid.org/0000-0003-0669-9126

Robert Moore − *Department of Chemistry, Virginia Polytechnic Institute and State University, Blacksburg, Virginia 24061, United States; Macromolecules Innovation Institute, Virginia Polytechnic Institute and State University, Blacksburg, Virginia 24061, United States;* orcid.org/0000-0001-9057-7695

Feng Lin − *Department of Chemistry, Virginia Polytechnic Institute and State University, Blacksburg, Virginia 24061, United States;* orcid.org/0000-0002-3729-3148

Complete contact information is available at: https://pubs.acs.org/10.1021/acssuschemeng.2c04750

Author Contributions

‖Q.J. and L.T. contributed equally.

Notes

The authors declare no competing financial interest.

https://doi.org/10.1021/acssuschemeng.2c04750
ACS Sustainable Chem. Eng. 2023, 11, 536−546

■ ACKNOWLEDGMENTS

This work was supported by the USDA AFRI Foundational and Applied Program, (Grant Number 2020-67021-31139), USA. H.H. acknowledges the support from the Virginia Agriculture Experiment Station, USA and the Hatch Program of the National Institute of Food and Agriculture (NIFA), USDA, USA. The cathode portion of the work was supported by the National Science Foundation under No. CBET 1912885. Purchase of the Xenocs Xeuss 3.0 SAXS/WAXS instrument used to obtain results included in this publication was supported by the National Science Foundation under the Award DMR MRI 2018258. Any opinions, findings, and conclusions or recommendations expressed in this material are those of the author(s) and do not necessarily reflect the views of the National Science Foundation.

■ REFERENCES

(1) Manthiram, A. An outlook on lithium ion battery technology. *ACS Cent. Sci.* **2017**, *3*, 1063−1069.
(2) Li, H.; Chuan, W.; Feng, W.; Ying, B. Sodium ion battery: A promising energy-storage candidate for supporting renewable electricity. *Acta Chim. Sin.* **2014**, *72*, 21−29.
(3) Palomares, V.; Serras, P.; Villaluenga, I.; Hueso, K. B.; Carretero-González, J.; Rojo, T. Na-ion batteries, recent advances and present challenges to become low cost energy storage systems. *Energy Environ. Sci.* **2012**, *5*, 5884−5901.
(4) Rahman, M. M.; Mao, J.; Kan, W. H.; Sun, C.-J.; Li, L.; Zhang, Y.; Avdeev, M.; Du, X.-W.; Lin, F. An ordered P2/P3 composite layered oxide cathode with long cycle life in sodium-ion batteries. *ACS Mater. Lett.* **2019**, *1*, 573−581.
(5) Rahman, M. M.; Zhang, Y.; Xia, S.; Kan, W. H.; Avdeev, M.; Mu, L.; Sokaras, D.; Kroll, T.; Du, X.-W.; Nordlund, D.; et al. Surface characterization of Li-substituted compositionally heterogeneous NaLi0. 045Cu0. 185Fe0. 265Mn0. 505O2 sodium-ion cathode material. *J. Phys. Chem. C* **2019**, *123*, 11428−11435.
(6) Rahman, M. M.; Xu, Y.; Cheng, H.; Shi, Q.; Kou, R.; Mu, L.; Liu, Q.; Xia, S.; Xiao, X.; Sun, C.-J.; et al. Empowering multicomponent cathode materials for sodium ion batteries by exploring three-dimensional compositional heterogeneities. *Energy Environ. Sci.* **2018**, *11*, 2496−2508.
(7) Hou, D.; Xia, D.; Gabriel, E.; Russell, J. A.; Graff, K.; Ren, Y.; Sun, C.-J.; Lin, F.; Liu, Y.; Xiong, H. Spatial and temporal analysis of sodium-ion batteries. *ACS Energy Lett.* **2021**, *6*, 4023−4054.
(8) Liu, Y.; Merinov, B. V.; Goddard, W. A. Origin of low sodium capacity in graphite and generally weak substrate binding of Na and Mg among alkali and alkaline earth metals. *Proc. Natl. Acad. Sci. U.S.A.* **2016**, *113*, 3735−3739.
(9) Stratford, J. M.; Kleppe, A. K.; Keeble, D. S.; Chater, P. A.; Meysami, S. S.; Wright, C. J.; Barker, J.; Titirici, M.-M.; Allan, P. K.; Grey, C. P. Correlating local structure and sodium storage in hard carbon anodes: insights from pair distribution function analysis and solid-state NMR. *J. Am. Chem. Soc.* **2021**, *143*, 14274−14286.
(10) Chen, X.; Tian, J.; Li, P.; Fang, Y.; Fang, Y.; Liang, X.; Feng, J.; Dong, J.; Ai, X.; Yang, H. An overall understanding of sodium storage behaviors in hard carbons by an "adsorption-intercalation/filling" hybrid mechanism. *Adv. Energy Mater.* **2022**, *12*, No. 2200886.
(11) Sun, N.; Guan, Z.; Liu, Y.; Cao, Y.; Zhu, Q.; Liu, H.; Wang, Z.; Zhang, P.; Xu, B. Extended "adsorption−insertion" model: a new insight into the sodium storage mechanism of hard carbons. *Adv. Energy Mater.* **2019**, *9*, No. 1901351.
(12) Surta, T. W.; Koh, E.; Li, Z.; Fast, D. B.; Ji, X.; Greaney, P. A.; Dolgos, M. R. Combining experimental and theoretical techniques to gain an atomic level understanding of the defect binding mechanism in hard carbon anodes for sodium ion batteries. *Adv. Energy Mater.* **2022**, *12*, No. 2200647.
(13) Wang, J.; Yan, L.; Ren, Q.; Fan, L.; Zhang, F.; Shi, Z. Facile hydrothermal treatment route of reed straw-derived hard carbon for high performance sodium ion battery. *Electrochim. Acta* **2018**, *291*, 188−196.
(14) Dou, X.; Hasa, I.; Hekmatfar, M.; Diemant, T.; Behm, R. J.; Buchholz, D.; Passerini, S. Pectin, hemicellulose, or lignin? Impact of the biowaste source on the performance of hard carbons for sodium-ion batteries. *ChemSusChem* **2017**, *10*, 2668−2676.
(15) Feng, Y.; Tao, L.; He, Y.; Jin, Q.; Kuai, C.; Zheng, Y.; Li, M.; Hou, Q.; Zheng, Z.; Lin, F.; Huang, H. Chemical-enzymatic fractionation to unlock the potential of biomass-derived carbon materials for sodium ion batteries. *J. Mater. Chem. A* **2019**, *7*, 26954−26965.
(16) Zhu, Y.-E.; Gu, H.; Chen, Y.-N.; Yang, D.; Wei, J.; Zhou, Z. Hard carbon derived from corn straw piths as anode materials for sodium ion batteries. *Ionics* **2018**, *24*, 1075−1081.
(17) Kim, N. R.; Yun, Y. S.; Song, M. Y.; Hong, S. J.; Kang, M.; Leal, C.; Park, Y. W.; Jin, H.-J. Citrus-peel-derived, nanoporous carbon nanosheets containing redox-active heteroatoms for sodium-ion storage. *ACS Appl. Mater. Interfaces* **2016**, *8*, 3175−3181.
(18) Cao, L.; Hui, W.; Xu, Z.; Huang, J.; Zheng, P.; Li, J.; Sun, Q. Rape seed shuck derived-lamellar hard carbon as anodes for sodium-ion batteries. *J. Alloys Compd.* **2017**, *695*, 632−637.
(19) Zhang, N.; Liu, Q.; Chen, W.; Wan, M.; Li, X.; Wang, L.; Xue, L.; Zhang, W. High capacity hard carbon derived from lotus stem as anode for sodium ion batteries. *J. Power Sources* **2018**, *378*, 331−337.
(20) Stojanovska, E.; Pampal, E. S.; Kilic, A.; Quddus, M.; Candan, Z. Developing and characterization of lignin-based fibrous nanocarbon electrodes for energy storage devices. *Composites, Part B* **2019**, *158*, 239−248.
(21) Chen, S.; Feng, F.; Ma, Z.-F. Lignin-derived nitrogen-doped porous ultrathin layered carbon as a high-rate anode material for sodium-ion batteries. *Compos. Commun.* **2020**, *22*, No. 100447.
(22) Du, L.; Wu, W.; Luo, C.; Xu, D.; Guo, H.; Wang, R.; Zhang, T.; Wang, J.; Deng, Y. Lignin-Derived nitrogen-doped porous carbon as a high-rate anode material for sodium ion batteries. *J. Electrochem. Soc.* **2019**, *166*, A423.
(23) Tao, L.; Zheng, Y.; Zhang, Y.; Di, M.; Zheng, Z. Flexible, ultrafine and abundant microporous carbon nanofibers prepared by electrospinning from resole-type liquefied biomass-based resin. *J. Porous Mater.* **2018**, *25*, 521−526.
(24) Lin, X.; Liu, Y.; Tan, H.; Zhang, B. Advanced lignin-derived hard carbon for Na-ion batteries and a comparison with Li and K ion storage. *Carbon* **2020**, *157*, 316−323.
(25) Peuvot, K.; Hosseinaei, O.; Tomani, P.; Zenkert, D.; Lindbergh, G. Lignin based electrospun carbon fiber anode for sodium ion batteries. *J. Electrochem. Soc.* **2019**, *166*, A1984.
(26) Jin, J.; Yu, B.-j.; Shi, Z.-q.; Wang, C.-y.; Chong, C.-b. Lignin-based electrospun carbon nanofibrous webs as free-standing and binder-free electrodes for sodium ion batteries. *J. Power Sources* **2014**, *272*, 800−807.
(27) Fidalgo, A.; Ciriminna, R.; Carnaroglio, D.; Tamburino, A.; Cravotto, G.; Grillo, G.; Ilharco, L. M.; Pagliaro, M. Eco-friendly extraction of pectin and essential oils from orange and lemon peels. *ACS Sustainable Chem. Eng.* **2016**, *4*, 2243−2251.
(28) Zhang, H.; Zhang, W.; Ming, H.; Pang, J.; Zhang, H.; Cao, G.; Yang, Y. Design advanced carbon materials from lignin-based interpenetrating polymer networks for high performance sodium-ion batteries. *Chem. Eng. J.* **2018**, *341*, 280−288.
(29) Li, Y.; Lu, Y.; Meng, Q.; Jensen, A. C.; Zhang, Q.; Zhang, Q.; Tong, Y.; Qi, Y.; Gu, L.; Titirici, M. M.; Hu, Y. Regulating pore structure of hierarchical porous waste cork-derived hard carbon anode for enhanced Na storage performance. *Adv. Energy Mater.* **2019**, *9*, No. 1902852.
(30) Inokuchi, H.; Nakagaki, M. The density of the poly cyclic aromatic compounds. *Bull. Chem. Soc. Jpn.* **1959**, *32*, 65−67.
(31) Ilavsky, J.; Jemian, P. R. Irena: tool suite for modeling and analysis of small-angle scattering. *J. Appl. Crystallogr.* **2009**, *42*, 347−353.
(32) Beaucage, G. Approximations leading to a unified exponential/power-law approach to small-angle scattering. *J. Appl. Crystallogr.* **1995**, *28*, 717−728.

https://doi.org/10.1021/acssuschemeng.2c04750
ACS Sustainable Chem. Eng. 2023, 11, 536−546

(33) Roe, R.-J.*Methods of X-ray and Neutron Scattering in Polymer Science*; Oxford University Press, 2000.
(34) Holoubek, J.; Yin, Y.; Li, M.; Yu, M.; Meng, Y. S.; Liu, P.; Chen, Z. Exploiting mechanistic solvation kinetics for dual-graphite batteries with high power output at extremely low temperature. *Angew. Chem.* **2019**, *131*, 19068−19073.
(35) Kim, C.; Yang, K. S.; Kojima, M.; Yoshida, K.; Kim, Y. J.; Kim, Y. A.; Endo, M. Fabrication of electrospinning-derived carbon nanofiber webs for the anode material of lithium-ion secondary batteries. *Adv. Funct. Mater.* **2006**, *16*, 2393−2397.
(36) Ghimbeu, C. M.; Górka, J.; Simone, V.; Simonin, L.; Martinet, S.; Vix-Guterl, C. Insights on the Na+ ion storage mechanism in hard carbon: Discrimination between the porosity, surface functional groups and defects. *Nano Energy* **2018**, *44*, 327−335.
(37) Zhu, Z.; Liang, F.; Zhou, Z.; Zeng, X.; Wang, D.; Dong, P.; Zhao, J.; Sun, S.; Zhang, Y.; Li, X. Expanded biomass-derived hard carbon with ultra-stable performance in sodium-ion batteries. *J. Mater. Chem. A* **2018**, *6*, 1513−1522.
(38) Chen, X.; Lv, L.-P.; Sun, W.; Hu, Y.; Tao, X.; Wang, Y. Ultrasmall MoC nanoparticles embedded in 3D frameworks of nitrogen-doped porous carbon as anode materials for efficient lithium storage with pseudocapacitance. *J. Mater. Chem. A* **2018**, *6*, 13705−13716.
(39) Hou, B. H.; Wang, Y. Y.; Ning, Q. L.; Li, W. H.; Xi, X. T.; Yang, X.; Liang, H. J.; Feng, X.; Wu, X. L. Self-supporting, flexible, additive-free, and scalable hard carbon paper self-interwoven by 1D microbelts: superb room/low-temperature sodium storage and working mechanism. *Adv. Mater.* **2019**, *31*, No. 1903125.
(40) Cao, Y.; Xiao, L.; Sushko, M. L.; Wang, W.; Schwenzer, B.; Xiao, J.; Nie, Z.; Saraf, L. V.; Yang, Z.; Liu, J. Sodium ion insertion in hollow carbon nanowires for battery applications. *Nano Lett.* **2012**, *12*, 3783−3787.
(41) Kumaresan, T. K.; Masilamani, S. A.; Raman, K.; Karazhanov, S. Z.; Subashchandrabose, R. High performance sodium-ion battery anode using biomass derived hard carbon with engineered defective sites. *Electrochim. Acta* **2021**, *368*, No. 137574.
(42) Stevens, D. A.; Dahn, J. An in situ small-angle X-ray scattering study of sodium insertion into a nanoporous carbon anode material within an operating electrochemical cell. *J. Electrochem. Soc.* **2000**, *147*, 4428.
(43) Bommier, C.; Surta, T. W.; Dolgos, M.; Ji, X. New mechanistic insights on Na-ion storage in nongraphitizable carbon. *Nano Lett.* **2015**, *15*, 5888−5892.
(44) Li, Y.; Chen, S.; Xu, S.; Wang, Z.; Yang, K.; Hu, J.; Cao, B.; Zhao, W.; Zhang, M.; Yang, L.; Pan, F. Impact of electrolyte salts on Na storage performance for high-surface-area carbon anodes. *ACS Appl. Mater. Interfaces* **2021**, *13*, 48745−48752.
(45) Fondard, J.; Irisarri, E.; Courreges, C.; Palacín, M. R.; Ponrouch, A.; Dedryvère, R. SEI composition on hard carbon in Na-ion batteries after long cycling: influence of salts (NaPF6, NaTFSI) and additives (FEC, DMCF). *J. Electrochem. Soc.* **2020**, *167*, No. 070526.
(46) Pan, Y.; Zhang, Y.; Parimalam, B. S.; Nguyen, C. C.; Wang, G.; Lucht, B. L. Investigation of the solid electrolyte interphase on hard carbon electrode for sodium ion batteries. *J. Electroanal. Chem.* **2017**, *799*, 181−186.
(47) Seh, Z. W.; Sun, J.; Sun, Y.; Cui, Y. A highly reversible room-temperature sodium metal anode. *ACS Cent. Sci.* **2015**, *1*, 449−455.
(48) Zhu, Y.; Wang, C. Galvanostatic intermittent titration technique for phase-transformation electrodes. *J. Phys. Chem. C* **2010**, *114*, 2830−2841.

https://doi.org/10.1021/acssuschemeng.2c04750
ACS Sustainable Chem. Eng. 2023, 11, 536−546